Physics-based and data-driven modeling of lava flows

Toluwanimi Akinwande [1], Kausik Das [2], Darsh Gandhi [3],
Maria Camila Mejia Garcia [4], Geoffrey Hewitt [5], Zhihua Li [6], Luan
Fabricio Lopes [7], Adam Petrucci [8], Isabelle Sanz [9], Hangjie Ji [*]

[1] *Claremont Graduate University, CA, USA*
[2] *University of Michigan, Ann Arbor, MI, USA*
[3] *The University of Texas at Arlington, TX, USA*
[4] *The University of Texas Rio Grande Valley,USA*
[5] *Claremont Graduate University, CA, USA*
[6] *University of Iowa, Iowa City, IA, USA*
[7] *Oklahoma State University, Stillwater, OK, USA*
[8] *Michigan State University, East Lansing, MI, USA*
[9] *Georgia Institute of Technology, Atlanta, GA, USA*
[*] *Mentor - North Carolina State University Raleigh, NC, USA.*

(*Communicated to* MIIR *on 11 June 2025*)

Study Group: Graduate Student Mathematical Modeling Camp, California State Polytechnic University, Pomona, June $4 - 7, 2025$.

Key Words: Lava flows, lubrication, asymptotics, temperature cooling, sensor placement

Summary

This project, presented by Hangjie Ji (Department of Mathematics, North Carolina State University) at the Graduate Student Mathematical Modeling Camp (GSMMC 2025), explores the dynamics of lava flows through a combination of physics-based modeling, numerical simulations, and data-driven sensor placement strategies. Lava flows pose major risks to communities and infrastructure, especially in volcanic regions with rising population density. We model this process by understanding how lava behaves as a gravity-driven viscous flow, influenced by factors such as:

(1) Topography and slope,
(2) Eruption conditions (effusion rate, vent geometry, initial temperature),
(3) Cooling effects and crust formation, and
(4) Thermal and physical properties of lava (e.g., viscosity, thermal conductivity).

A variety of simplified models are introduced, including 1D isoviscous flow models and spreading flows on inclined planes, with emphasis on how lava cooling and effusion rate (including time-dependent rates) impact spreading dynamics. These models are solved using numerical methods, particularly finite difference methods, to approximate the behavior of lava over time, incorporating a temperature profile to capture the cooling of lava as it spreads. The coupling of thermal and flow models enhances physical realism and provides deeper insight into the evolution of lava domes and flows. We use similarity solutions and asymptotic analysis to aid in the theoretical understanding of such flows.

The project also explores how to reconstruct lava flow thermal video from a limited number of sensors. We develop and contrast two data-driven strategies. The first is a stationary method that uses SVD and QR decomposition on an offline training dataset to find a single, fixed set of optimal sensor locations. While effective, this approach is inflexible if the lava flow evolves significantly. To address this, we introduce a dynamical method that adapts sensor locations in real-time. Crucially, this method operates online without requiring access to the full global data, instead learning from a sliding window of recent sparse measurements. This adaptive strategy proves more flexible at tracking the flow, though its responsiveness to rapid events is linked to its parameters, revealing key challenges for real-time monitoring.

1 Introduction

Volcanic activity poses a significant threat to human life and society. In the past quarter century alone, despite modern forecasting and prevention procedures, volcanic eruptions accounted for over eight hundred lives lost and two and a half billions US dollars in damages [23]. Moreover, long-term consequences of volcanic eruptions on human health include a variety of severe respiratory conditions, to which infants and children are particularly vulnerable [12]. This threat is of global relevance, as nearly 600,000,000 people live within 100 kilometers from an eruptive volcano [13].

As such natural disasters are currently beyond the scope of direct human intervention, the priority is on preventing damage and injury following an eruption event. These measures include the establishment of evacuation protocols at both regional and local levels [25], and consistent monitoring of potential volcanic activity [24, 32].

Optimal implementation of these efforts requires a thorough understanding of the physics involved in volcanic eruptions. In particular, accurate models for lava flows, which pose some of the most immediate danger in an eruption event, are of the utmost importance. In conjunction, sensor placement for the monitoring of lava flows is critical to both developing models and advising live-response to volcanic activity. All told, an understanding of lava flows is key to the protection of life and property in the event of a volcanic eruption.

The islands of Hawai'i feature many active volcanoes whose lava flows are useful for constructing and validating models. The pantheon of Hawai'ian volcanoes includes such prominent examples as the Kilauea, Mauana Kea, and Mauana Loa volcanoes [36]. Kilauea is among the most active volcanoes on the planet, erupting almost continuously between 1983 and 2018. Hawaiian volcanoes are typically shield volcanoes, which are large, wide volcanoes constructed by thin lava flows over long periods of time. They experience effusive eruptions, meaning hot magma does not spew out far into the sky and lava flows down volcanic slopes easily.

The shape and roughness of lava flow help determine lava properties [33]. Lava flow is dependent on viscosity and the terrain or path upon which it moves. Further, lava viscosity depends on silica content, temperature, and shear rate [30]. Higher silica content and lower temperature correspond to higher viscosity in lava. Basaltic magmas, like those produced by the shield volcanoes of Hawai'i, have relatively little silica and an intermediate temperature (1000-1200°C) [28], leading to a low viscosity. Due to the size of shield volcanoes and their gentle, convex slopes, lava can flow quickly down these volcanoes. Such eruptions are especially dangerous, so are of the greatest interest to model.

Lava flows exhibit a wealth of distinct behaviors, admitting a variety of interrelated models [15]. One approach, especially useful in predicting the thickness of a flow, adapts the Navier-Stokes equations according to lubrication theory [26] to interpret the fluid dynamics as a free boundary problem. This was applied to the study of axisymmetric flows and used to model the development of a two-dimensional lava dome with both constant and variables effusion rates from a point source [17]. These ideas were extended to consider time-dependent effusion from both point and line sources on an inclined plane

[20]. Within the more generalized framework, solutions exhibited distinct short-time and long-time behaviors.

Various forms of sensors are used to track, model, and forecast volcanic activity. Satellites can monitor gas, thermal, and ash emissions as well as surface changes and deformation due to the destructive movement and cooling of lava [29]. Thermal infrared sensors can capture the escape of hot air and gases out of vents and lava flows down channels [7]. Further, remote thermal infrared sensors can provide imaging of lava flows that are hidden behind volcanic smoke and plume. Visible light sensors, compared to thermal infrared sensors, cannot capture as much information about flowing lava; for example, thermal infrared sensors can supply temperature data corresponding to different colors in the image, while visible light cameras can only capture lava flow incandescence at night and will not provide associated temperature data [9]. Volcanologists also use seismometers to detect seismic activity before, during, and after volcanic eruptions and tremors [22]. Strategic placement of seismometers, cameras, and other sensors are crucial for extracting important volcanic data quickly and is key for providing volcano warnings to people in areas which could be affected.

Some previous studies have investigated optimal sensor placement for volcano monitoring [31, 16, 19, 27], but few have looked into mathematically optimal sensor placement. The optimal sensor placement problem can be equivalently formulated as a fluid flow reconstruction problem if given video/imaging data during an eruption. Many mathematical studies have investigated fluid flow reconstruction from sparse data [4, 2, 3, 1, 14, 37] using methods such as proper orthogonal decomposition (POD) and dynamic mode decomposition (DMD). Chaturantubut and Sorensen proposed the POD DEIM algorithm for nonlinear model order reduction [5, 6] and many have applied this methodology for reconstructing fluid flow [10, 35, 18]. In [11], Farazmand and Saibaba proposed a tensor-based approach for flow estimation and sensor placement from sparse data as opposed to a vector-based approach investigated in [8, 21]. In this report, we apply some of these techniques (specifically POD-DEIM and vector-based flow estimation) to reconstruct images of lava flow from volcanic sources and determine the optimal location of sensors.

The rest of the report is organized as follows: Section 2 presents the physics-based modeling, asymptotic analysis, and numerical simulation of lava flow down an inclined plane. Section 3 discusses optimal sensor placement strategies for lava flow image data and presents numerical results of the proposed algorithms. Concluding remarks are presented in Section 4.

2 Physics-based modeling

In this section, we first derive a lubrication model for a thin viscous lava flow flowing down an inclined plane in Subsection 2.1. Analysis for asymptotically self-similar solutions describing lava flow profiles in short and long time limits are presented in Subsection 2.2. Numerical simulations of the lava profile with and without temperature cooling dynamics are discussed in Subsection 2.3 and Subsection 2.4, respectively.

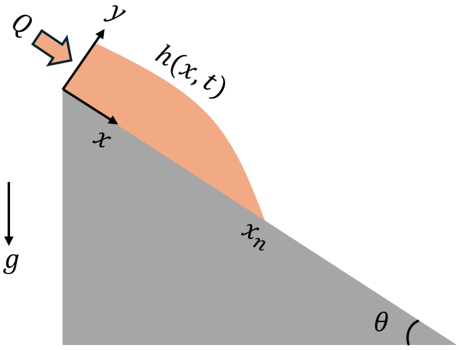

Figure 1. Schematic of inclined lava flow.

2.1 Lubrication Approximation of Lava Flow

Modeling lava flow down an incline of angle θ (see Figure 1) requires lubrication theory. Because lava is a highly viscous fluid (Re $\ll$ 1), the Navier-Stokes equations in two dimensions reduce to the Stokes equations:

$$\frac{\partial u}{\partial x} + \frac{\partial v}{\partial y} = 0, \tag{2.1}$$

$$\nu\left(\frac{\partial^2 u}{\partial x^2} + \frac{\partial^2 u}{\partial y^2}\right) + g\sin\theta - \frac{1}{\rho}\frac{\partial p}{\partial x} = 0, \tag{2.2}$$

$$\nu\left(\frac{\partial^2 v}{\partial x^2} + \frac{\partial^2 v}{\partial y^2}\right) - g\cos\theta - \frac{1}{\rho}\frac{\partial p}{\partial y} = 0. \tag{2.3}$$

where u is the fluid velocity in the x-direction, v is the fluid velocity in the y-direction, ρ is the fluid density, ν is the fluid kinematic viscosity, and $p(x, y, t)$ is the fluid pressure. Equation (2.1) is known as the continuity equation, and equations (2.2) and (2.3) are the x and y momentum equations, respectively.

To nondimensionalize the equations, two length scales are introduced: H, the average film thickness, and L, the incline scale in the flow direction. The lubrication theory approximation assumes that

$$\epsilon = \frac{H}{L} \ll 1. \tag{2.4}$$

Additional dimensionless variables can be introduced:

$$\tilde{u} = \frac{u}{gH^2/\nu}, \quad \tilde{v} = \frac{v}{V}, \quad \tilde{p} = \frac{p}{\rho g L}, \quad \tilde{x} = \frac{x}{L}, \quad \tilde{y} = \frac{y}{H}, \quad \tilde{t} = \frac{t}{\nu L/gH^2}, \tag{2.5}$$

where V is the undetermined longitudinal velocity scale. In terms of the dimensionless variables, the incompressibility equation becomes

$$\epsilon\frac{gH^2}{\nu V}\frac{\partial \tilde{u}}{\partial \tilde{x}} + \frac{\partial \tilde{v}}{\partial \tilde{y}} = 0. \tag{2.6}$$

For the terms to balance, we require $\epsilon g H^2/\nu V = O(1)$ such that $V = \epsilon g H^2/\nu$. With this scaling applied, the momentum equations now become

$$\epsilon^2 \frac{\partial^2 \tilde{u}}{\partial \tilde{x}^2} + \frac{\partial^2 \tilde{u}}{\partial \tilde{y}^2} + \sin\theta - \frac{\partial \tilde{p}}{\partial \tilde{x}} = 0, \tag{2.7}$$

$$\epsilon^4 \frac{\partial^2 \tilde{v}}{\partial \tilde{x}^2} + \epsilon^2 \frac{\partial^2 \tilde{v}}{\partial \tilde{y}^2} - \epsilon\cos\theta - \frac{\partial \tilde{p}}{\partial \tilde{y}} = 0. \tag{2.8}$$

Dropping $O(\epsilon^2)$ terms and higher yields the lubrication approximation

$$\frac{\partial \tilde{u}}{\partial \tilde{x}} + \frac{\partial \tilde{v}}{\partial \tilde{y}} = 0, \tag{2.9}$$

$$\frac{\partial^2 \tilde{u}}{\partial \tilde{y}^2} + \sin\theta - \frac{\partial \tilde{p}}{\partial \tilde{x}} = 0, \tag{2.10}$$

$$\frac{\partial \tilde{p}}{\partial \tilde{y}} = -\epsilon\cos\theta. \tag{2.11}$$

Furthermore, the no-slip boundary condition (BC) is imposed at the surface of the incline $\tilde{y} = 0$, and the tangential stress balance BC is imposed at the air-lava interface $\tilde{y} = \tilde{h}(x,t)$:

$$\tilde{u}(\tilde{x}, \tilde{y} = 0, \tilde{t}) = 0, \quad \tilde{v}(\tilde{x}, \tilde{y} = 0, \tilde{t}) = 0, \tag{2.12}$$

$$\frac{\partial \tilde{u}}{\partial \tilde{y}}(\tilde{x}, \tilde{y} = \tilde{h}(\tilde{x}, \tilde{t}), \tilde{t}) = 0. \tag{2.13}$$

Integrating (2.11) with respect to $\tilde{y}$ and applying the BC $\tilde{p}(\tilde{x}, \tilde{y} = \tilde{h}(\tilde{x}, \tilde{t}), \tilde{t}) = 0$ results in the pressure

$$\tilde{p}(\tilde{x}, \tilde{y}, \tilde{t}) = \epsilon\cos\theta(\tilde{h}(\tilde{x}, \tilde{t}) - \tilde{y}). \tag{2.14}$$

Substituting the pressure expression into (2.10), integrating twice with respect to $\tilde{y}$, and applying the BCs gives

$$\tilde{u}(\tilde{x}, \tilde{y}, \tilde{t}) = \left(\frac{\tilde{y}^2}{2} - h\tilde{y}\right)\left(\frac{\partial \tilde{p}}{\partial \tilde{x}} - \sin\theta\right). \tag{2.15}$$

By mass conservation, the lava-air interface is governed by

$$\frac{\partial \tilde{h}}{\partial \tilde{t}} + \frac{\partial}{\partial \tilde{x}}\left[\int_0^{\tilde{h}} \tilde{u}(x,y,t)\, d\tilde{y}\right] = 0. \tag{2.16}$$

Inserting the formula into (2.16) produces the final form:

$$\frac{\partial \tilde{h}}{\partial \tilde{t}} - \frac{\epsilon\cos\theta}{12}\frac{\partial^2 \tilde{h}^4}{\partial \tilde{x}^2} + \frac{\sin\theta}{3}\frac{\partial \tilde{h}^3}{\partial \tilde{x}} = 0. \tag{2.17}$$

2.2 Similarity Solution of Lava Profile

In order to obtain a similarity solution to the PDE modeling inclined lava flow, we begin by introducing a scaling change of variables for the dimensional version of (2.17) with equation

$$\frac{\partial h}{\partial t} - \frac{g\cos\theta}{12\nu}\frac{\partial^2 h^4}{\partial x^2} + \frac{g\sin\theta}{3\nu}\frac{\partial h^3}{\partial x} = 0, \tag{2.18}$$

and a one-dimensional (line) variable flux source BC

$$\int_0^{x_n} h(x,t)\,dx = Qt^{\alpha}, \tag{2.19}$$

where Q and α are prescribed constants and x_n marks the layer's zero-height edge location. We denote $\beta = g\cos\theta/12\nu$, and $\gamma = g\sin\theta/3\nu$ in (2.18). This problem formulation represents a reduced-order model of the two-dimensional version found in the work of Lister [20]. The scaling change of variables for the lava layer's height, its length, and time are respectively defined as

$$h = \mathbf{H}\,\overline{h}, \qquad x = \mathbf{L}\,\overline{x}, \qquad t = \mathbf{T}\,\overline{t}, \tag{2.20}$$

where $\mathbf{H}$, $\mathbf{L}$, and $\mathbf{T}$ represent the dimensional scaling constants—or characteristic scales; $\overline{h}$, $\overline{x}$, and $\overline{t}$ represent the dimensionless variables.

The first step is to determine whether this problem is scale invariant, meaning whether there exists a choice of characteristic scales such that the dimensional PDE and BC for h can be equivalently written as a dimensionless PDE and BC for $\overline{h}$. The benefit of scale invariant problems is that they can have similarity solutions—solutions where the characteristic scales are related so their variables have no dependence on the free scaling parameter. Similarity solutions are usually easier to derive and provide key characteristic behavior of the problem's system. Given scale invariance, relations between the characteristic scales can be established, which determine the form of the similarity solution from resulting scale-invariant (S-I) groups. The similarity solution for $h(x,t)$ can then be substituted back into the original problem to produce a reduced problem in the form of an ODE for the similarity profile function $f(\eta)$.

To check for scale invariance, substitute the scaling change of variables into (2.18) and (2.19) and group the characteristic scales:

$$\begin{gathered} \frac{\partial\overline{h}}{\partial\overline{t}} - \beta \underbrace{\frac{\mathbf{H}^3\mathbf{T}}{\mathbf{L}^2}}_{\text{Coeff. 1}} \frac{\partial^2\overline{h}^{\,4}}{\partial\overline{x}^{\,2}} + \gamma \underbrace{\frac{\mathbf{H}^2\mathbf{T}}{\mathbf{L}}}_{\text{Coeff. 2}} \frac{\partial\overline{h}^{\,3}}{\partial\overline{x}} = 0, \\ \underbrace{\frac{\mathbf{H}\mathbf{L}}{\mathbf{T}^{\alpha}}}_{\text{Coeff. 3}} \int_0^{x_n} \overline{h}\,d\overline{x} = Q\overline{t}^{\alpha}. \end{gathered} \tag{2.21}$$

There are two possible sets of scaling relations formed from the three coefficients in (2.21); coefficient 3 must be included in both sets of scaling relations to ensure consistent adherence to the BC.

2.2.1 *Short-term similarity solution*

One set of scaling relations involves balancing coefficients 1 and 3 in (2.21):

$$\frac{\mathbf{H}^3\mathbf{T}}{\mathbf{L}^2} = 1, \qquad \frac{\mathbf{H}\mathbf{L}}{\mathbf{T}^{\alpha}} = 1. \tag{2.22}$$

An S-I group can be formed from the relations in (2.22) to determine the similarity solution:

$$\mathbf{L} \sim \mathbf{T}^{\frac{3\alpha+1}{5}}, \quad \mathbf{H} \sim \mathbf{T}^{\frac{2\alpha-1}{5}}, \tag{2.23}$$

$$\eta = xt^{-\frac{3\alpha+1}{5}}, \qquad h = t^{\frac{2\alpha-1}{5}} f(\eta). \tag{2.24}$$

Substituting this similarity solution for $h(x,t)$ back into the original problem of (2.18) and (2.19) results in the following ODE:

$$\left(\frac{2\alpha-1}{5}\right) f(\eta) - \left(\frac{3\alpha+1}{5}\right) \eta f'(\eta) - 4\beta\left[f^3(\eta)f'(\eta)\right]' + \underbrace{3\gamma t^{\frac{\alpha+2}{5}} f^2(\eta)f'(\eta)}_{\text{Asymptotic Term}} = 0, \tag{2.25}$$

Because as $t \to 0$, the asymptotic term $\to 0$, the final form of the similarity ODE drops this term and represents a leading-order solution valid for the short-term:

$$\left(\frac{2\alpha-1}{5}\right) f(\eta) - \left(\frac{3\alpha+1}{5}\right) \eta f'(\eta) - 4\beta\left[f^3(\eta)f'(\eta)\right]' = 0, \tag{2.26}$$

for $\alpha > 0$.

$\alpha = 0$ corresponds to constant volume, and $\alpha = 1$ corresponds to constant flux. Positive values of α less than or greater than 1 correspond to time-varying flux. The time t exponent associated with the asymptotic term in (2.25) matches the corresponding asymptotic term exponent of the two-dimensional representation derived in [20], verifying that this analytical model captures some expected system dynamics.

Because the short-term ODE (2.26) is a second-order equation, two boundary conditions are required. To determine what these are, the original PDE (2.18) can be thought of in a form storing the time variation and flux of the system:

$$\frac{\partial h}{\partial t} + \frac{\partial q}{\partial x} = 0, \tag{2.27}$$

where q is the system flux. Comparing (2.27) with (2.26) considered in the original dimensional space implies that

$$q = -\beta \frac{\partial h^4}{\partial x}. \tag{2.28}$$

Taking the time derivative of (2.19) we have

$$\frac{\partial}{\partial t}\int_0^{x_n} h(x,t)\, dx = \alpha Q t^{\alpha-1} = q(0,t), \tag{2.29}$$

giving the BC for h as

$$h^3 \left.\frac{\partial h}{\partial x}\right|_{x=0} = -\frac{\alpha Q t^{\alpha-1}}{4\beta}. \tag{2.30}$$

Substituting in the expression for h from (2.24) into (2.30) to obtain the BC relation for $f(\eta)$ results in

$$f^3(0)f'(0) = -\frac{\alpha Q}{4\beta}. \tag{2.31}$$

The leading-order similarity ODE (2.26) with its corresponding BCs was implemented in a MATLAB script to solve for $f(\eta)$. It was numerically integrated using `ode45`. Given

$f(0)$, the initial condition $f'(0)$ was obtained using (2.31) and the value of Q was chosen such that $f(\eta)$ had a positive root, marking the layer's zero-height edge location x_n.

Figure 2 depicts a solution for $f(\eta)$ with parameters $\theta = 0.4, Q = 0.2791, f(0) = 1, \alpha = 1.1$. Physically, this figure represents a case where a volcanic vent releases an increasing lava flux over time since $\alpha > 1$. This results in a relatively limited spread of the lava down the incline—denoted by the small range for η, which agrees with expected behavior for a very viscous fluid. Overall, the plot exhibits qualitative agreement with plots produced in the work of Huppert et al. [17] for radial flows.

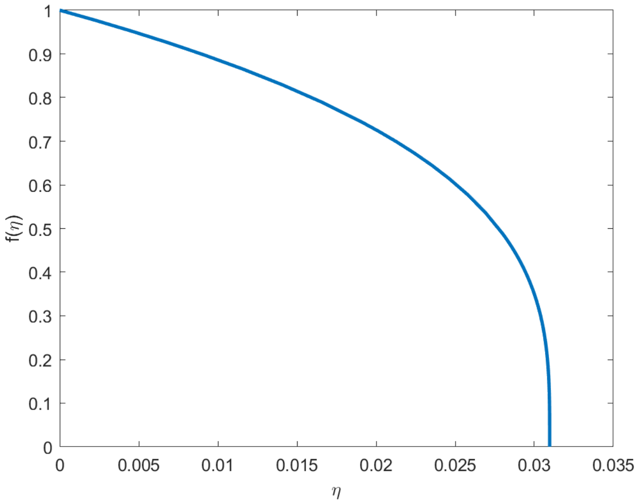

Figure 2. Short-term solution for $f(\eta)$ for $\theta = 0.4, Q = 0.2791, f(0) = 1, \alpha = 1.1$.

2.2.2 *Long-term similarity solution*

The other set of scaling relations involves balancing coefficients 2 and 3 in (2.21):

$$\frac{\mathbf{H}^2\mathbf{T}}{\mathbf{L}} = 1, \qquad \frac{\mathbf{HL}}{\mathbf{T}^\alpha} = 1. \tag{2.32}$$

An S-I group can be formed from the relations in (2.32) to determine the long-term similarity solution:

$$\mathbf{L} \sim \mathbf{T}^{\frac{2\alpha+1}{3}}, \quad \mathbf{H} \sim \mathbf{T}^{\frac{\alpha-1}{3}}, \tag{2.33}$$

$$\eta = xt^{-\frac{2\alpha+1}{3}}, \qquad h = t^{\frac{\alpha-1}{3}} f(\eta). \tag{2.34}$$

Substituting the long-term similarity solution for $h(x,t)$ back into the original problem of (2.18) and (2.19) results in the following ODE:

$$\left(\frac{\alpha-1}{3}\right) f(\eta) - \left(\frac{2\alpha+1}{3}\right) \eta f'(\eta) \underbrace{-4\beta t^{-\frac{\alpha+2}{3}} \left[f^3(\eta) f'(\eta)\right]'}_{\text{Asymptotic Term}} + 3\gamma f^2(\eta) f'(\eta) = 0. \tag{2.35}$$

Because as $t \to \infty$, the asymptotic term $\to 0$, the final form of the similarity ODE drops this term and represents a leading-order solution valid for the long-term:

$$\left(\frac{\alpha-1}{3}\right) f(\eta) - \left(\frac{2\alpha+1}{3}\right) \eta f'(\eta) + 3\gamma f^2(\eta) f'(\eta) = 0, \tag{2.36}$$

for $\alpha > 0$.

Once again, the time t exponents associated with the asymptotic term in (2.35) matches the corresponding asymptotic term exponent of the two-dimensional representation derived in [20].

Because the leading order ODE (2.36) is a first-order equation, one boundary condition is required. An equivalent procedure for determining the short-term similarity ODE BCs is applied here. Comparing (2.27) with (2.36) considered in the original dimensional space implies that

$$q = \gamma h^3. \tag{2.37}$$

By (2.29):

$$\alpha Q t^{\alpha-1} = \gamma \left. h^3 \right|_{x=0}, \tag{2.38}$$

giving the BC for h as

$$h(0,t) = \left[\frac{\alpha Q t^{\alpha-1}}{\gamma}\right]^{\frac{1}{3}}. \tag{2.39}$$

Substituting in the expression for h from (2.34) into (2.39) to obtain the BC relation for $f(\eta)$ results in

$$f(0) = \left(\frac{\alpha Q}{\gamma}\right)^{\frac{1}{3}}. \tag{2.40}$$

The leading-order similarity ODE (2.36) with its corresponding BC was numerically solved for $f(\eta)$ using MATLAB. It was numerically integrated using `ode45`. Figure 3 shows the long-term solution for $f(\eta)$ for various values of α with $Q = 1$ and $\theta = 0.2$. Note that solutions cannot be computed for the full domain due to a singularity in the (2.36) occurring when

$$f(\eta) = \left[\frac{(2\alpha+1)\eta}{9\gamma}\right]^{1/2}. \tag{2.41}$$

Physically, this figure represents a qualitative study of a volcanic vent releasing various levels of increasing lava flux over time since $\alpha \geq 1$. For larger values of α—meaning, those that account for larger increasing flux levels—the lava experiences less spread down the incline. This observation agrees with expected behavior for a very viscous fluid because as more volume is released, the fluid ”sticks” to itself, increasingly hindering its ability to spread easily. It is as if the vent essentially becomes increasingly clogged with more lava release. This means that for smaller values of α, more spread will be observed. Thus the overall trend shows a receding spread with larger levels of increasing lava flux. This plot exhibits qualitative agreement with those shown in [20].

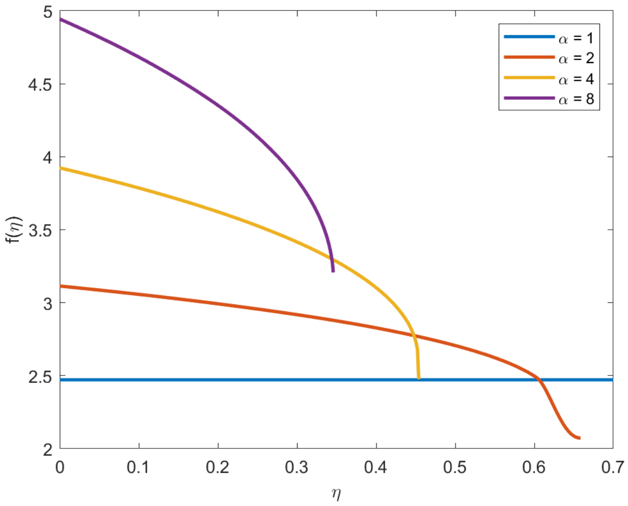

Figure 3. Long-term solution for $f(\eta)$ for $\alpha = 1, 2, 4, 8$ when $Q = 1$ and $\theta = 0.2$.

2.3 Numerical Approximation of Lava Profile

The dimensional form of equation (2.17) is:

$$\frac{\partial h}{\partial t} - \frac{g\cos\theta}{12\nu}\frac{\partial^2 h^4}{\partial x^2} + \frac{g\sin\theta}{3\nu}\frac{\partial h^3}{\partial x} = 0 \tag{2.42}$$

When the angle of the inclined plane approaches zero, equation (2.42) becomes a second-order nonilnear diffusion equation modeling the spreading of liquid on a flat substrate fluid:

$$\frac{\partial h}{\partial t} - \frac{g}{12\nu}\frac{\partial^2 h^4}{\partial x^2} = 0. \tag{2.43}$$

We apply second-order central finite differences and forward Euler method to numerically simulate the PDEs (2.42) and (2.43) using a uniform spatial grid of size Δx and time step Δt. The finite difference discretization at the grid point (x_j, t_n) yields

$$\frac{\partial h}{\partial t} \approx \frac{h_j^{n+1} - h_j^n}{\Delta t}, \quad \frac{\partial h}{\partial x} \approx \frac{h_{j+1}^n - h_{j-1}^n}{2\Delta x}, \quad \frac{\partial^2 h}{\partial x^2} \approx \frac{h_{j+1}^n - 2h_j^n + h_{j-1}^n}{\Delta x^2}, \tag{2.44}$$

where h_j^n represents the lava/air interface at spatial position x_j and time step t_n. This yields the following discrete equations for PDEs (2.42) and (2.43), respectively:

$$h_j^{n+1} = h_j^n + \Delta t \frac{g}{12\nu}\Big(\frac{{h_{j+1}^n}^4 - 2{h_j^n}^4 + {h_{j-1}^n}^4}{\Delta x^2}\Big), \tag{2.45}$$

$$\begin{aligned} h_j^{n+1} = h_j^n + \cos\theta\Delta t \frac{g}{12\nu}\Big(\frac{{h_{j+1}^n}^4 - 2{h_j^n}^4 + {h_{j-1}^n}^4}{\Delta x^2}\Big) \\ - \sin\theta\Delta t \frac{g}{6\nu}\Big(\frac{{h_{j+1}^n}^3 - {h_{j-1}^n}^3}{\Delta x}\Big) \end{aligned} \tag{2.46}$$

2.4 Numerical Approximation of the Temperature Field

Given the lava flow profile, the lava eventually cools as it spreads. To model this thermal behavior, we introduce a temperature distribution governed by the heat equation:

$$\frac{\partial T}{\partial t} = k\frac{\partial^2 T}{\partial x^2}, \tag{2.47}$$

where $T(x,t)$ is the temperature at location x and time t, and k is the thermal conductivity of the lava. This partial differential equation captures the diffusion of heat through the lava. To solve the equation (2.47) numerically, we apply finite differences again. Let T_j^n denote the temperature at the spatial position x_j and time step t_n, $T_j^n \approx T(x_j, t_n)$. Applying forward Euler in time and central finite difference in space to equation (2.47), we obtain the discretization for the temperature field in a one-dimensional space:

$$T_j^{n+1} = T_j^n + \frac{k\Delta t}{\Delta x^2}\left(T_{j+1}^n - 2T_j^n + T_{j-1}^n\right). \tag{2.48}$$

Figure 4 presents a typical temperature distribution obtained from simulating the one-dimensional heat equation (2.47) within a given fluid body domain defined by $y = h(x,t)$, $y = 0$, and $0 \leq x \leq x_n$.

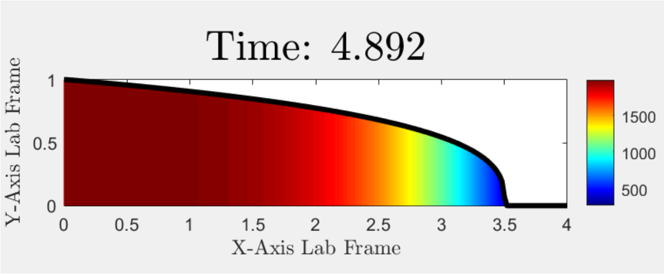

Figure 4. A typical temperature profile obtained by solving the one-dimensional heat equation (2.47) within a prescribed lava fluid domain.

A more accurate model for the temperature profile can be described in a two-dimensional space. To describe and numerically solve for the temperature profile in 2D, we consider the two-dimensional heat equation

$$\frac{\partial T}{\partial t} = k\Big(\frac{\partial^2 T}{\partial x^2} + \frac{\partial^2 T}{\partial y^2}\Big) \tag{2.49}$$

and the corresponding finite difference discretization

$$T_{i,j}^{n+1} = T_{i,j}^n + k\Delta t\Big(\frac{T_{i+1,j}^n - 2T_{i,j}^n + T_{i-1,j}^n}{\Delta x^2} + \frac{T_{i,j+1}^n - 2T_{i,j}^n + T_{i,j-1}^n}{\Delta y^2}\Big), \tag{2.50}$$

where $T_{i,j}^n \approx T(x_i, y_j, t_n)$. This explicit finite-difference scheme can be used to simulate the temperature evolution of the lava over time, allowing us to track how the lava cools while flowing down the incline. The numerical results will be shown and discussed in Subsection 2.6 of this report.

2.5 Stability Considerations

Since the forward Euler time-stepping is used to solve the lava flow dynamics, one needs to discuss the stability constraints on the time step Δt. We obtain stability restrictions for equations (2.42) and (2.43) using Von-Neumann analysis.

Let $h_j^n = G^n e^{ij\Delta x}$ and define $a = g/12\nu\Delta x^2$. Substituting $h_j^n = G^n e^{ij\Delta x}$ into equation (2.45), we obtain

$$G^{n+1}e^{ij\Delta x} = G^n e^{ij\Delta x} + \frac{g\Delta t}{12\nu\Delta x^2}\left[\left(G^n\right)^4 e^{4i(j+1)\Delta x} - 2\left(G^n\right)^4 e^{4ij\Delta x} + \left(G^n\right)^4 e^{4i(j-1)\Delta x}\right].$$

Dividing both sides by $G^n e^{ij\Delta x}$ gives:

$$\frac{G^{n+1}}{G^n} = 1 + a\Delta t\left(G^n\right)^3 e^{3ij\Delta x}\left(e^{4i\Delta x} - 2 + e^{-4i\Delta x}\right).$$

The stability condition for the numerical scheme (2.45) is given by

$$\left|1 + a\Delta t\, h_m^3\left(e^{4i\Delta x} - 2 + e^{-4i\Delta x}\right)\right| \leq 1, \tag{2.51}$$

where $h_m = \max_{n,j} G^n e^{ij\Delta x}$. Using Euler's identity $e^{4i\Delta x} + e^{-4i\Delta x} = 2\cos(4\Delta x)$, we reduce the inequality (2.51) to

$$-1 \leq 1 + a\Delta t\, h_m^3(2\cos(4\Delta x) - 2) \leq 1.$$

Since $-1 \leq \cos(4\Delta x) \leq 1$, the worst case gives the constraints on the time step Δt:

$$1 - 4a\Delta t\, h_m^3 \geq -1 \quad\Rightarrow\quad \Delta t \leq \frac{1}{2ah_m^3} \quad\Rightarrow\quad \Delta t \leq \frac{6\nu\Delta x^2}{gh_m^3}.$$

Stability restrictions are found in a similar fashion for equation (2.43),

$$h_j^{n+1} = h_j^n - \beta(\theta)\frac{\Delta t}{2\Delta x}\left(\left(h_{j+1}^n\right)^3 - \left(h_{j-1}^n\right)^3\right) + \gamma(\theta)\frac{\Delta t}{\Delta x^2}\left(\left(h_{j+1}^n\right)^4 - 2\left(h_j^n\right)^4 + \left(h_{j-1}^n\right)^4\right) \tag{2.52}$$

where

$$\gamma(\theta) = \frac{g\cos\theta}{12\nu}, \qquad \beta(\theta) = \frac{g\sin\theta}{3\nu}$$

We also define

$$c(\theta) = \frac{\gamma(\theta)}{\Delta x^2}, \qquad s(\theta) = \frac{\beta(\theta)}{2\Delta x}, \qquad h_j^n = G^n e^{ij\Delta x}.$$

Substituting in equation (2.52), we obtain

$$G^{n+1}e^{ijx} = G^n e^{ijx} + c(\theta)\Delta t\left[\left(G^n\right)^4 e^{4i(j+1)\Delta x} - 2\left(G^n\right)^4 e^{4ij\Delta x} + \left(G^n\right)^4 e^{4i(j-1)\Delta x}\right]$$
$$-s(\theta)\Delta t\left[\left(G^n\right)^3 e^{3i(j+1)\Delta x} - \left(G^n\right)^3 e^{3i(j-1)\Delta x}\right].$$

To guarantee the stability of the numerical scheme, we need $\left|G^{n+1}/G^n\right| \leq 1$, which leads to

$$\left|1 + c(\theta)\Delta t\, h_m^3\left(2\cos(4\Delta x) - 2\right) - 2i\, s(\theta)\Delta t\, h_m^2\sin(3\Delta x)\right| \leq 1,$$

where $h_m = \max_{n,j} G^n e^{ij\Delta x}$ is the maximum height of the free interface. This inequality yields the constraint on the time step Δt

$$\Delta t \leq -\frac{gh_{\mathrm{m}}^2}{3\nu}\left(\frac{\sin\theta\sin(3\Delta x)}{\Delta x} + \frac{\cos\theta h_m}{4(\Delta x)^2}(\cos(4\Delta x) - 1)\right).$$

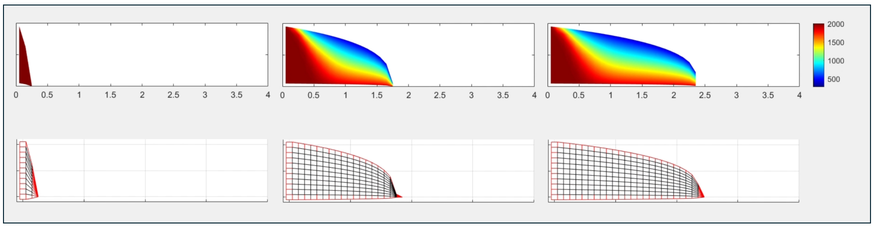

Figure 5. Snapshots of lava flow dynamics over a flat substrate with temperature cooling.

2.6 Numerical Results

The following boundary and initial conditions are applied to the lava flow profile illustrated in Figure 1:

$$h(0,t) = 1 \quad \text{(Dirichlet condition at the left boundary)} \tag{2.53}$$

$$h(x_N,t) \approx 0 \quad \text{(Dirichlet condition at the right boundary)} \tag{2.54}$$

$$h(x,0) = \begin{cases} 1, & \text{for } x = 0 \text{ and } x = \Delta x \\ 0, & \text{otherwise} \end{cases} \tag{2.55}$$

For the heat equation (2.49), the following boundary conditions are applied to the temperature profile $T(x,y,t)$:

$$T(0,y,t) = T_{\text{high}}, \quad 0 < y < 1,\ t > 0 \tag{2.56}$$

$$T(x,h(x),t) = T_{\text{low}}, \quad 0 < x < x_n(t),\ t > 0 \tag{2.57}$$

$$T(x,0,t) = T_{\text{high}}, \quad 0 < x < x_n(t)\ t > 0,\ t > 0, \tag{2.58}$$

where T_{high} and T_{low} are the lava temperature at the inlet and the ambient temperature, respectively. In numerical simulations, we set $T_{\text{high}} = 2000$ and $T_{\text{low}} = 0$. To handle the moving contact line at $x = x_n(t)$, we regenerate a new spatial grid using the updated profile modeled from equations (2.42) or (2.43) every time the lava profile $y = h(x)$ evolves. If the contact line of the lava profile shifts more than a distance of Δx, the entire temperature profile is shifted to the right to simulate a uniform velocity. Numerical simulation of the lava flow with temperature cooling with zero and 0.2 radian incline angles at three different times are shown in Figure 5 and Figure 6. Time constraints precluded the development of an algorithm to solve for the 2D viscous velocity profile, which we note would have provided much more accurate position updates for the temperature field.

3 Optimal sensor placement

Next, we switch gear to discuss the optimal sensor placement problem for lava flow thermal images. Specifically, we discuss stationary optimal sensor placement strategies in Subsection 3.1 and the dynamical strategies in subsection 3.2. Numerical results are presented in Subsection 3.3.

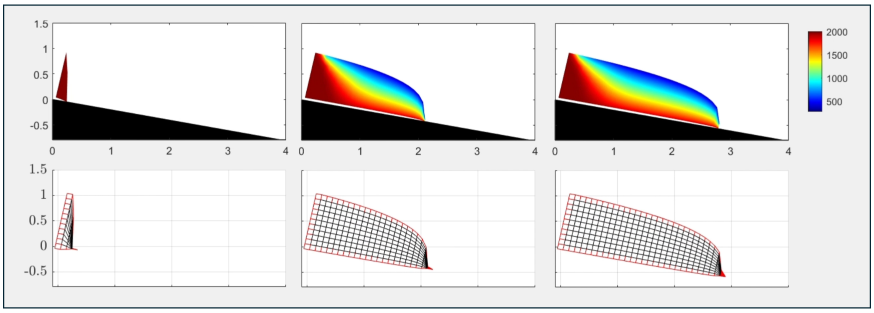

Figure 6. Snapshots of lava flow dynamics over an inclined plane at 0.2 radian angle with temperature cooling.

3.1 Stationary Optimal Sensor Placement and Reconstruction from Sparse Measurements of All Time

In an ideal scenario, the optimal sensor placement problem could be solved deterministically if we had perfect knowledge of the system's governing partial differential equations and access to complete snapshots of the entire physical field. However, acquiring such comprehensive snapshots is rarely a trivial process. For instance, during a volcanic eruption, crucial areas of the lava flow may be permanently or temporarily obscured by dense volcanic smoke and ash clouds, or blocked from view by the surrounding topography, making a complete measurement of the field at any given moment unattainable.

Meanwhile in reality, the full profile of the lava flow is usually not accessible, since we have a limited budget and also a limited number of sensors to monitor the lava flow dynamics. Therefore, we are interested in the optimal way to place the limited number of sensors for reconstructing the full field. More precisely, we address the reconstruction of a high-dimensional data matrix $\mathbf{G} \in \mathbb{R}^{N\times T}$ from r sparse measurements, where $r \ll N$. These measurements are acquired via a sparse row-selection matrix,

$$\mathbf{S}^T \in \mathbb{R}^{r\times N}, \tag{3.1}$$

whose rows are distinct standard basis vectors $\mathbf{e}_j^T$. The product $\mathbf{S}^T\mathbf{G}$ thus represents the extraction of r specific rows (sensor readings) from $\mathbf{G}$. Our objective is to find a reasonable $\mathbf{S}^\mathbf{T}$ that represents the stationary optimal placement of the sensors, and to design a linear reconstruction operator, $\mathbf{R} \in \mathbb{R}^{N\times r}$, which forms the reconstructed data

$$\mathbf{G}_{recon} = \mathbf{R}(\mathbf{S}^T\mathbf{G}). \tag{3.2}$$

We can firstly address the second question, to find reconstruction operator $\mathbf{R}$ if $\mathbf{S}^\mathbf{T}$ is already given. The aspiration is for $\mathbf{G}_{recon}$ to be the best possible rank-r approximation of $\mathbf{G}$ in the Frobenius norm $\|\cdot\|_F$.

To establish a theoretical target for this best approximation, we refer to the Eckart-Young-Mirsky theorem. This theorem states that for any matrix $\mathbf{G}$ with singular value decomposition (SVD) $\mathbf{G} = \mathbf{U\Sigma V}^T = \sum_{i=1}^{\text{rank}(\mathbf{G})} \sigma_i \mathbf{u}_i \mathbf{v}_i^T$, its best rank-$r$ approximation, $\mathbf{G}_r$, is given by the first r terms of its SVD:

$$\mathbf{G}_r = \mathbf{U}_r\mathbf{\Sigma}_r\mathbf{V}_r^T = \sum_{i=1}^{r} \sigma_i \mathbf{u}_i \mathbf{v}_i^T. \tag{3.3}$$

Here, $\mathbf{U}_r = [\mathbf{u}_1|\dots|\mathbf{u}_r] \in \mathbb{R}^{N\times r}$ contains the first r left singular vectors, which also form the Proper Orthogonal Decomposition (POD) basis [2]. An equivalent and useful expression for $\mathbf{G}_r$ is

$$\mathbf{G}_r = \mathbf{U}_r(\mathbf{U}_r^T\mathbf{G}) \tag{3.4}$$

where we consider $\mathbf{U}_r$ to be the basis and $\mathbf{U}_r^T\mathbf{G}$ the coordinates obtained through projection or inner product. This matrix $\mathbf{G}_r$ uniquely minimizes $\|\mathbf{G}-\mathbf{X}\|_F$ over all matrices $\mathbf{X}$ where $\operatorname{rank}(\mathbf{X}) \leq r$. The minimum error achieved, representing the information lost by truncation, is

$$\|\mathbf{G}-\mathbf{G}_r\|_F^2 = \sum_{i=r+1}^{\operatorname{rank}(\mathbf{G})} \sigma_i^2. \tag{3.5}$$

Thus, $\mathbf{G}_r$ serves as the ideal theoretical target for our rank-r reconstruction $\mathbf{G}_{recon}$.

A direct attempt to make our reconstruction $\mathbf{G}_{recon} = \mathbf{R}\mathbf{S}^T\mathbf{G}$ equal to this ideal $\mathbf{G}_r = \mathbf{U}_r\mathbf{U}_r^T\mathbf{G}$ for all $\mathbf{G}$ would require the operator equality

$$\mathbf{R}\mathbf{S}^T = \mathbf{U}_r\mathbf{U}_r^T. \tag{3.6}$$

However, this equality generally fails if $\mathbf{S}^T$ is a sparse row-selection matrix and $N > r$. The reason is structural: $\mathbf{R}\mathbf{S}^T$ would inherently possess $N-r$ zero columns (corresponding to unmeasured rows), whereas the orthogonal projector $\mathbf{U}_r\mathbf{U}_r^T \in \mathbb{R}^{N\times N}$ (rank r) is typically dense (maybe all elements and thus columns are nonzero). Consequently, perfectly recovering $\mathbf{G}_r$ for all $\mathbf{G}$ is generally not feasible with a linear reconstruction from sparse, point-wise measurements if we insist on this strict operator identity.

Given this limitation in achieving the ideal $\mathbf{G}_r$ directly through operator equality (3.6) with sparse sensors, we construct $\mathbf{G}_{recon}$ by enforcing two physically and mathematically motivated conditions:

(a) The reconstruction $\mathbf{G}_{recon}$ must lie in the optimal r-dimensional subspace $\operatorname{span}\{\mathbf{U}_r\}$. This is motivated by the fact that $\mathbf{G}_r$, our target, resides entirely in this subspace. This implies

$$\mathbf{G}_{recon} = \mathbf{U}_r\mathbf{A} \tag{3.7}$$

for some coefficient matrix $\mathbf{A} \in \mathbb{R}^{r\times T}$ in the $\mathbf{U}_r$ basis.

(b) The reconstruction must be consistent with the actual sensor measurements. This means if we were to "measure" our reconstructed field $\mathbf{G}_{recon}$ with the same sensors $\mathbf{S}^T$, we should obtain the original measurements $\mathbf{S}^T\mathbf{G}$:

$$\mathbf{S}^T\mathbf{G}_{recon} = \mathbf{S}^T\mathbf{G}. \tag{3.8}$$

To find $\mathbf{A}$, we substitute (3.7) into (3.8), yielding $\mathbf{S}^T(\mathbf{U}_r\mathbf{A}) = \mathbf{S}^T\mathbf{G}$. This leads to the linear system for $\mathbf{A}$:

$$(\mathbf{S}^T\mathbf{U}_r)\mathbf{A} = \mathbf{S}^T\mathbf{G}. \tag{3.9}$$

The $r \times r$ matrix $\mathbf{S}^T\mathbf{U}_r$ consists of the r rows of $\mathbf{U}_r$ selected by $\mathbf{S}^T$. If this matrix is invertible, we can determine $\mathbf{A}$ as

$$\mathbf{A} = (\mathbf{S}^T\mathbf{U}_r)^{-1}\mathbf{S}^T\mathbf{G}. \tag{3.10}$$

Substituting this $\mathbf{A}$ back into $\mathbf{G}_{recon} = \mathbf{U}_r\mathbf{A}$, the reconstruction becomes

$$\mathbf{G}_{recon} = \mathbf{U}_r(\mathbf{S}^T\mathbf{U}_r)^{-1}\mathbf{S}^T\mathbf{G}. \tag{3.11}$$

From this form, we identify the linear reconstruction operator $\mathbf{R}$ as

$$\mathbf{R} = \mathbf{U}_r(\mathbf{S}^T\mathbf{U}_r)^{-1}. \tag{3.12}$$

Therefore, $\mathbf{R}$ is uniquely determined once $\mathbf{S}$ (the sensor locations) and $\mathbf{U}_r$ (the data-driven basis) are fixed. This reconstruction approach is based on the Discrete Empirical Interpolation Method (DEIM) [5].

The derived form of the reconstruction operator, $\mathbf{R} = \mathbf{U}_r(\mathbf{S}^T\mathbf{U}_r)^{-1}$, highlights that the selection of the sparse row-selection matrix $\mathbf{S}^T$ is a critical step. For $\mathbf{R}$ to be well-defined and for the reconstruction to be numerically stable, the $r \times r$ matrix $\mathbf{S}^T\mathbf{U}_r$ must not only be invertible but also well-conditioned. A well-conditioned $\mathbf{S}^T\mathbf{U}_r$ ensures that the norm of its inverse, $\|(\mathbf{S}^T\mathbf{U}_r)^{-1}\|_2$, is not excessively large. This control over the inverse norm is essential to prevent significant amplification of measurement noise or modeling inaccuracies during the reconstruction process.

The task thus shifts to finding a suitable $\mathbf{S}^T \in \mathbb{R}^{r\times N}$. The invertibility of $\mathbf{S}^T\mathbf{U}_r$ is equivalent to the invertibility of its transpose, which is $(\mathbf{S}^T\mathbf{U}_r)^T = \mathbf{U}_r^T\mathbf{S}$. Therefore, the matrix $\mathbf{U}_r^T\mathbf{S}$ is formed by selecting r specific columns from $\mathbf{U}_r^T \in \mathrm{Re}^{r\times N}$. Notably, the selection matrix $\mathbf{S}$ itself can be viewed as a sub-matrix of an $N \times N$ permutation matrix, specifically, the part that picks out r columns. For this, we employ the column-pivoted QR factorization algorithm on $\mathbf{U}_r^T$, a technique widely used for sparse sensor selection in data-driven modeling [21]. This algorithm is well-suited for identifying a set of "most linearly independent" columns from a given matrix. When applied to $\mathbf{U}_r^T$, it produces a factorization where the full permutation matrix $\mathbf{P} \in \mathbb{R}^{N\times N}$ is partitioned into two blocks: $\mathbf{P} = [\mathbf{P}_1|\mathbf{P}_2]$. Here, $\mathbf{P}_1 \in \mathbb{R}^{N\times r}$ consists of the first r columns of $\mathbf{P}$ that select the desired columns, and $\mathbf{P}_2 \in \mathbb{R}^{N\times(N-r)}$ contains the remaining columns.

This partitioning explicitly highlights the selection process within the QR decomposition:

$$[\mathbf{U}_r^T\mathbf{P}_1|\mathbf{U}_r^T\mathbf{P}_2] = \mathbf{U}_r^T[\mathbf{P}_1|\mathbf{P}_2] = \mathbf{U}_r^T\mathbf{P} = \mathbf{Q}[\mathbf{R}_{11}|\mathbf{R}_{12}] = [\mathbf{Q}\mathbf{R}_{11}|\mathbf{Q}\mathbf{R}_{12}], \tag{3.13}$$

where $\mathbf{Q} \in \mathbb{R}^{r\times r}$ is an orthogonal matrix, and the right-hand side is an upper trapezoidal matrix with $\mathbf{R}_{11} \in \mathbb{R}^{r\times r}$ being upper triangular and non-singular.

By equating the corresponding blocks, we see the dual roles of the permutation. The full permutation $\mathbf{P}$ reorders the entire column space of $\mathbf{U}_r^T$. Crucially, its first block $\mathbf{P}_1$ acts as our selection matrix, $\mathbf{S} = \mathbf{P}_1$. This leads to the key relationship for the selected columns:

$$\mathbf{U}_r^T\mathbf{S} = \mathbf{Q}\mathbf{R}_{11}. \tag{3.14}$$

The column pivoting strategy within the QR algorithm is designed to maximize the volume spanned by the selected columns, which ensures that $\mathbf{R}_{11}$ is well-conditioned. Since $\mathbf{Q}$ is orthogonal (and thus invertible) and $\mathbf{R}_{11}$ is invertible by construction, their product $\mathbf{U}_r^T\mathbf{S}$ is also invertible. Consequently, the matrix of interest, $\mathbf{S}^T\mathbf{U}_r = (\mathbf{U}_r^T\mathbf{S})^T = \mathbf{R}_{11}^T\mathbf{Q}^T$, is also invertible and tends to be well-conditioned. The procedure is detailed in Algorithm 1.

Algorithm 1 Column-Pivoted QR for Sensor Selection (acting on $\mathbf{A}_0 = \mathbf{U}_r^T$)

```
Input: $\mathbf{A}_0 = \mathbf{U}_r^T \in \mathbb{R}^{r \times N}$ (transpose of POD basis); number of sensors $r$.
Output: Selection matrix $\mathbf{S} \in \mathbb{R}^{N \times r}$ .
Initialize permutation matrix $\mathbf{P} \leftarrow \mathbf{I}_N$. Let working matrix $\mathbf{A} \leftarrow \mathbf{A}_0$.
for $k = 1$ to $r$ do
    Pivot Selection: Among columns $\mathbf{A}_{:,k}, \dots, \mathbf{A}_{:,N}$ of the current $A$, find column index $j_{\text{pivot}}$ (its original index in $A_0$ is tracked by $\mathbf{P}$) corresponding to the column with the largest Euclidean norm.
    Swap column $k$ of $\mathbf{A}$ with column $j_{\text{pivot}}$ of $\mathbf{A}$.
    Swap column $k$ of $\mathbf{P}$ with column $j_{\text{pivot}}$ of $\mathbf{P}$ (this records the permutation of original column indices).
    Householder Reflection: Determine a Householder vector $\mathbf{v}_k$ for the $k$-th column of the current $A$ (specifically for its sub-vector $A_{k:r,k}$) to zero out elements below the $k$-th diagonal element $A_{k,k}$.
    Apply the corresponding Householder reflection $H_k = (\mathbf{I} - 2\frac{\mathbf{v}_k \mathbf{v}_k^T}{\|\mathbf{v}_k\|_2^2})$ to the submatrix $A_{k:r,k:N}$.
    (The matrix $\mathbf{Q}$ is implicitly formed by the product of $H_k$'s; the modified $A$ progressively becomes $\mathbf{R}_{qr}$).
end for
```

This selection process, implemented via column-pivoted QR factorization, aims to select columns of $\mathbf{U}_r^T$ (which correspond to rows of $\mathbf{U}_r$) that are “most” linearly independent so that we can pick out part of the subsequent $\mathbf{P}$ to be our sensor selection strategy $\mathbf{S^T}$. This, in turn, makes the crucial matrix $\mathbf{S}^T\mathbf{U}_r$ well-conditioned, enabling the stable and effective application of the derived reconstruction operator $\mathbf{R} = \mathbf{U}_r(\mathbf{S}^T\mathbf{U}_r)^{-1}$ for robust data reconstruction from sparse measurements.

An important remark is that the stationary sensor placement strategy is entirely data-dependent. The determination of the selection matrix $\mathbf{S}^T$ follows a direct dependency chain: $\mathbf{G} \rightarrow \mathbf{U}_r \rightarrow \mathbf{S}^T$, and then to $\mathbf{R}$. Specifically, the snapshot matrix $\mathbf{G}$ is first used to compute the POD basis $\mathbf{U}_r$, which in turn dictates the optimal sensor locations. Consequently, the resulting sensor configuration is intrinsically determined by the specific dynamics captured in the original lava flow snapshots of all time.

3.2 Dynamical Optimal Sensor Placement and Reconstruction from Real Time Sparse Measurements

The aforementioned methodology determines an optimal sensor placement that is static in time. This approach, while effective for a given dataset, presents two primary challenges when considering real-world, ongoing applications.

First, the method constitutes an offline learning process. To determine the single optimal sensor configuration $\mathbf{S}$, it requires access to the entire data matrix $\mathbf{G}$ spanning all time instances. Such a setup is more akin to a post-processing analysis of a fully collected dataset. The resulting static placement $\mathbf{S}$ is fixed once it is computed from $\mathbf{G}$. The hope is that this placement strategy might offer some utility for economically reconstructing future flows at the same physical location, assuming statistical stationarity. However, any update to this sensor placement would necessitate a new, complete time-series sample of the global field $\mathbf{G}$.

Second, the computation of the optimal basis $\mathbf{U}_r$ requires access to the full-field data. In experimental contexts, such as our use of video data from the 2020–2021 summit eruption of Kilauea volcano, Island of Hawai'i, provided by the USGS, the pixel information is analogous to having the entire flow field. This presents a practical contradiction: to find an optimal sparse sensing strategy $\mathbf{S}$, we first need access to the complete, non-sparse field information, the acquisition of which is often prohibitively expensive.

The limitations of the stationary approach motivate a new framework for *Dynamical Optimal Sensor Placement and Reconstruction from Real-Time Sparse Measurements.* The intuition arises from the previously established logical process of identifying the optimal sensor placement $\mathbf{G} \to \mathbf{U}_r \to \mathbf{S}$. Meanwhile, the sensor placement $\mathbf{S}$ itself guides how we sample the field to produce a reconstruction ($\mathbf{S} \to \mathbf{R} \,\&\, \mathbf{G}_{\text{sampled}} \to \mathbf{G}_{recon}$). We conjecture that these two processes can be linked to form a closed-loop update scheme, $\mathbf{S}_t \to \cdots \to \mathbf{S}_{t+1}$, that adapts in real-time. This dynamical framework is characterized by the following principles:

(1) **Online Learning.** The sensor placement $\mathbf{S}_t$ is constructed and updated dynamically and online, potentially from a random initial state. It is time-varying and learns adaptively. Crucially, the process of learning $\mathbf{S}_t$ relies less on external information, such as requiring a sample of the whole field $\mathbf{G}_t$ at each step, and more on the sparse measurements $\mathbf{S}_{t-1}^T\mathbf{G}_{t-1}$ and the subsequent reconstruction.

(2) **Window Sliding.** The reason for using a sliding window of recent reconstructions, $\mathbf{G}_{recon,\text{window}}$, to guide the sensor placement $\mathbf{S}$ is that this window contains the most current available information on the flow's dynamics, and we desire the sensor placement to adapt to these recent changes. The use of a window is also motivated by a key constraint on the system's rank.

The decision-making basis $\mathbf{U}_{r,\text{local}}$ for $\mathbf{S}$ is computed from this window matrix $\mathbf{G}_{recon,\text{window}} \in \mathrm{Re}^{N\times W}$ using SVD. The rank of this basis is therefore limited by the rank of the window matrix, which in turn is limited by its number of columns W. This relationship can be expressed as a chain of inequalities:

$$\operatorname{rank}(\mathbf{U}_{r,\text{local}}) \leq \operatorname{rank}(\mathbf{G}_{recon,\text{window}}) \leq \min(N, W). \tag{3.15}$$

In typical scenarios where the number of pixels N far exceeds the window size W, this simplifies to $\operatorname{rank}(\mathbf{G}_{recon,\text{window}}) \leq W$. To effectively utilize r sensors to identify r distinct modes of the system, the decision basis $\mathbf{U}_{r,\text{local}} \in \mathrm{Re}^{N\times r}$ must be of full rank, i.e.,

$$\operatorname{rank}(\mathbf{U}_{r,\text{local}}) = r. \tag{3.16}$$

Combining these conditions, we have $r = \operatorname{rank}(\mathbf{U}_{r,\text{local}}) \leq \operatorname{rank}(\mathbf{G}_{recon,\text{window}}) \leq W$, which leads to the necessary constraint on the window size:

$$W \geq r. \tag{3.17}$$

This provides the fundamental motivation for employing a sliding window. It math-

Algorithm 2 Dynamical Optimal Sensor Placement and Reconstruction from Real-Time Sparse Measurements

```
Input: True data snapshots (optional, for simulation) $\mathbf{G}_{\text{true}} \in \mathbb{R}^{N \times T_{total}}$; Number of exploitation sensors $r_{\text{exploit}}$; Number of exploration (scout) sensors $r_{\text{explore}}$; Sliding window size $W$; Global basis truncation rank $r_{\text{global}}$.
Output: Reconstructed data snapshots $\mathbf{G}_{\text{recon}} \in \mathbb{R}^{N \times T_{total}}$; History of sensor locations $\{\mathbf{S}_t\}_{t=1}^{T_{total}}$; Reconstruction errors $\{\epsilon_t\}_{t=1}^{T_{total}}$.
Phase 1: Offline Training
Compute a global, robust basis $\mathbf{U}_{r,\text{global}} \in \mathbb{R}^{N \times r_{\text{global}}}$ from a comprehensive historical dataset $\mathbf{G}_{\text{train}}$ via SVD: $\mathbf{G}_{\text{train}} \approx \mathbf{U}_{r,\text{global}} \mathbf{\Sigma}_{r,\text{global}} \mathbf{V}_{r,\text{global}}^T$.
Phase 2: Online Adaptive Placement and Reconstruction
Initialize:
Set sliding window of recent reconstructions $\mathcal{W} \leftarrow \{\mathbf{0}_{N\times 1}, \ldots, \mathbf{0}_{N\times 1}\}$ (size $W$).
Initialize exploitation sensor locations $\mathcal{P}_{\text{exploit}} \subset \{1, \ldots, N\}$ by selecting $r_{\text{exploit}}$ random indices. $|\mathcal{P}_{\text{exploit}}| = r_{\text{exploit}}$.
for $t = 1$ to $T_{total}$ do
    (a) Determine Current Sensor Placement $\mathbf{S}_t$
    Determine exploration sensor locations $\mathcal{P}_{\text{explore}}$ by randomly sampling $r_{\text{explore}}$ indices from $\{1, \ldots, N\} \setminus \mathcal{P}_{\text{exploit}}$.
    Combine sensor sets: $\mathcal{P}_t \leftarrow \mathcal{P}_{\text{exploit}} \cup \mathcal{P}_{\text{explore}}$.
    Construct the sparse measurement matrix $\mathbf{S}_t^T \in \mathbb{R}^{(r_{\text{exploit}}+r_{\text{explore}})\times N}$ from indices in $\mathcal{P}_t$.
    (b) Perform Measurement and Reconstruction
    Acquire sparse measurements from the true field at time $t$: $\mathbf{y}_t = \mathbf{S}_t^T \mathbf{g}_{\text{true},t}$.
    Define the time-dependent reconstruction operator $\mathbf{R}_{\text{global},t}$ using the global basis:
    $\mathbf{R}_{\text{global},t} \coloneqq \mathbf{U}_{r,\text{global}} (\mathbf{S}_t^T \mathbf{U}_{r,\text{global}})^{-1}$.
    Compute the reconstructed field using the operator: $\mathbf{g}_{\text{recon},t} = \mathbf{R}_{\text{global},t} \mathbf{y}_t$.
    (c) Record Results and Update History
    Store the reconstructed field $\mathbf{g}_{\text{recon},t}$.
    Calculate reconstruction error $\epsilon_t = \|\mathbf{g}_{\text{true},t} - \mathbf{g}_{\text{recon},t}\| / \|\mathbf{g}_{\text{true},t}\|$.
    Update the sliding window: remove the oldest reconstruction and add $\mathbf{g}_{\text{recon},t}$ to $\mathcal{W}$.
    (d) Adapt for Next Time Step
    Form the snapshot matrix from the window history: $\mathbf{G}_{\text{window}} = $ [reconstructions in $\mathcal{W}$].
    Compute a local basis $\mathbf{U}_{r,\text{local}}$ from $\mathbf{G}_{\text{window}}$ via SVD, with rank $r_{\text{exploit}}$.
    Determine the next set of exploitation sensor locations $\mathcal{P}_{\text{exploit}}$ by applying column-pivoted QR factorization to $\mathbf{U}_{r,\text{local}}^T$: $[\sim, \sim, P] = \text{qr}(\mathbf{U}_{r,\text{local}}^T)$.
    Update $\mathcal{P}_{\text{exploit}} \leftarrow P(1 : r_{\text{exploit}})$.
end for
```

ematically explains why a window(single frame) size of $W = 1$ is insufficient—as it leads to a rank-1 basis and subsequent sensor clustering—and dictates that the history used for decision-making must be at least as rich as the number of adaptive sensors.

(3) **Randomness for Exploration and a Global Basis for Reconstruction.** A purely adaptive feedback loop, $\mathbf{S}_t \rightarrow \mathbf{G}_{recon,t}(\mathbf{G}_{recon,\text{window}}) \rightarrow \mathbf{S}_{t+1} \rightarrow \ldots$, is susceptible to premature convergence to a suboptimal placement (”self-locking”) or instability from poor reconstructions. To mitigate this, we introduce two mechanisms. First, to prevent the sensor placement $\mathbf{S}_t$ from becoming permanently locked onto a local feature, a portion of the sensors are designated as random ”scouts”, embedded within $\mathbf{S}_t$ at each time step. These scouts are selected from the global set of locations and ensure persistent exploration. Second, to prevent the reconstruction quality from degrading and corrupting the feedback loop, the reconstruction step itself consistently uses a robust, global basis, $\mathbf{U}_{r,\text{global}}$, that was pre-trained on a comprehensive historical dataset. This ensures reconstruction stability while the sensor placement remains agile and adaptive.

A detailed procedure is detailed in Algorithm 2.

3.3 Numerical Experiments of Optimal Sensor Placement

To validate the proposed sensor placement methodologies, we apply them to real-world thermal imagery from a volcanic eruption. This section details the data preparation, the results from the stationary placement strategy, and followed by the simulations for the dynamical approach.

3.3.1 *Stationary Sensor Placement*

The practical implementation begins with data acquisition and processing. Our dataset is a time-lapse thermal video sequence recorded by the U.S. Geological Survey’s Hawaiian Volcano Observatory [34], capturing activity at the Halema’uma’u crater between February 7 and 10, 2022.

First, the video was preprocessed to remove extraneous elements such as timestamps and color scales. We extracted a total of $T = 462$ grayscale frames. Each frame was then reshaped into a column vector by flattening its pixel values, and these vectors were organized to form the data matrix $\mathbf{G} \in \mathbb{R}^{N\times T}$, where $N = 1,493,096$ is the total number of pixels per frame. This matrix was then divided equally into a training set, $\mathbf{G}_{\text{train}}$, and a testing set, $\mathbf{G}_{\text{test}}$.

To identify the dominant spatial features of the lava flow, we applied singular value decomposition (SVD) to the training matrix:

$$\mathbf{G}_{\text{train}} = \mathbf{U}\mathbf{\Sigma}\mathbf{V}^T \approx \mathbf{U}_r\mathbf{\Sigma}_r\mathbf{V}_r^T,$$

where the columns of $\mathbf{U}_r$ represent the most energetic spatial modes (POD basis). The rapid decay of the singular values, shown in Figure 7, confirms that a low-dimensional

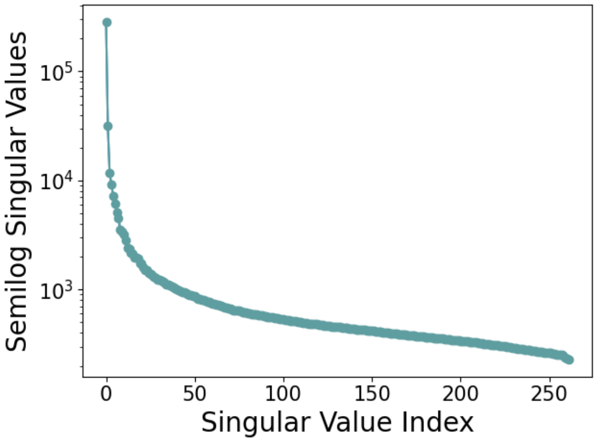

Figure 7. Spectrum of singular values from $\mathbf{G}_{\text{train}}$ on a logarithmic scale. The sharp decay indicates that the system's energy is concentrated in the first few modes.

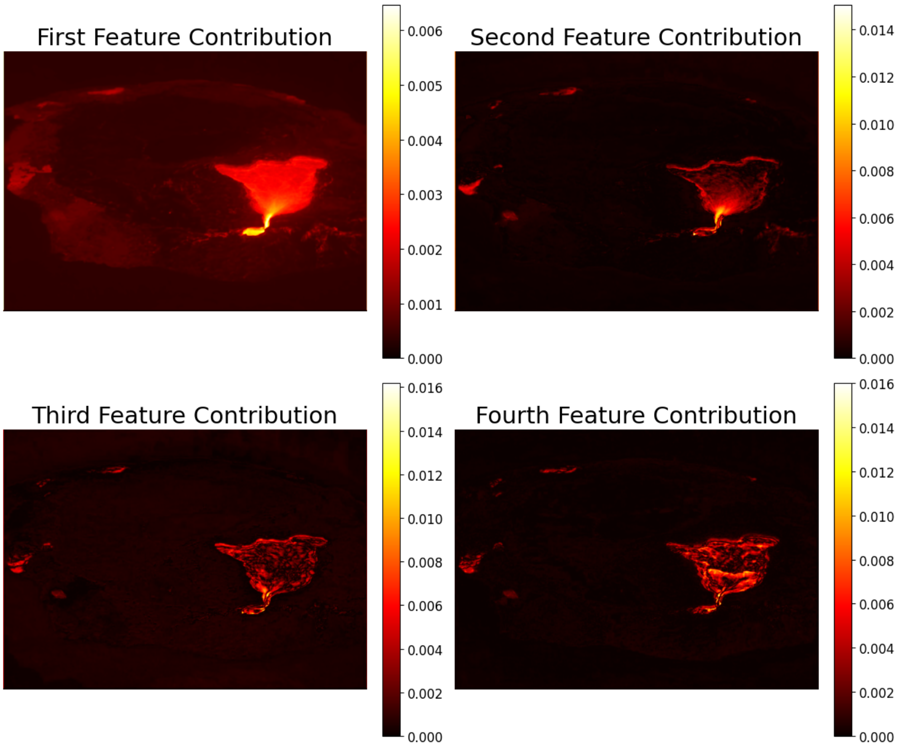

Figure 8. Visualization of the first four SVD spatial modes (columns of $\mathbf{U}_r$). These modes highlight the most persistent and energetic regions of lava activity.

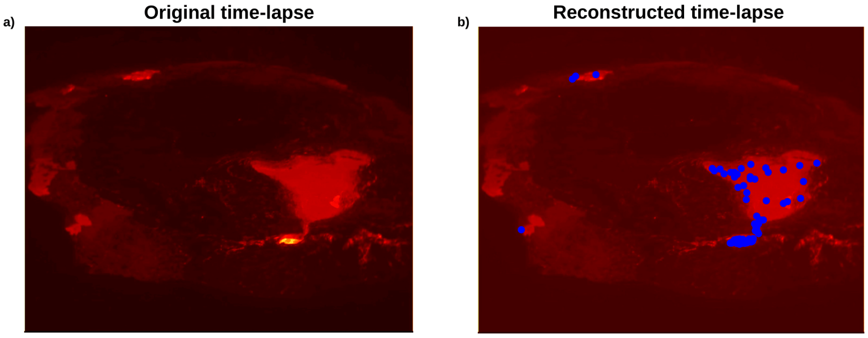

Figure 9. Comparison of the original time-lapse (left) with the reconstructed time-lapse (right) using $r = 100$ optimally placed stationary sensors.

representation can capture most of the data's variance, justifying the use of a truncated basis.

By reshaping the columns of $\mathbf{U}_r$ back into image dimensions, we can visualize these dominant spatial patterns. Figure 8 displays the first four modes, where bright regions correspond to pixels with the most significant contribution to the flow's dynamics, such as the active vents and lava lake entry points.

Following the theory from Section 3.1, the optimal sensor locations for this stationary basis were determined by applying a column-pivoted QR decomposition to $\mathbf{U}_r^T$. This method selects the pixel locations that best span the feature space captured by the basis. Using the measurements from these selected locations on the test data, we reconstructed the entire thermal video sequence. Figure 9 compares the original footage with the reconstructed sequence using $r = 100$ sensors, demonstrating a high-fidelity reconstruction from sparse measurements.

A closer examination of the thermal footage reveals two distinct dynamical phases, roughly corresponding to the periods before and after a major eruption event. In the latter phase, the lava covers a significantly broader area. We observe that the stationary algorithm, though trained on the entire dataset, identifies optimal points that are predominantly located within the regions active during the first phase. This suggests a limitation of the static approach: it is biased towards the initial, more localized dynamics and lacks the flexibility to account for significant spatial evolution of the flow over time. We will see this limitation partially addressed by the dynamical placement strategy in the following section.

3.3.2 *Dynamical Sensor Placement Simulation*

We now implement the dynamical algorithm from Section 3.2 on the same lava flow dataset. This approach utilizes a hybrid strategy: sensor locations are determined adaptively based on a sliding window of recent reconstructions (local sensing), but the field reconstruction itself is performed using a fixed, pre-trained global basis (global reconstruction) to ensure stability.

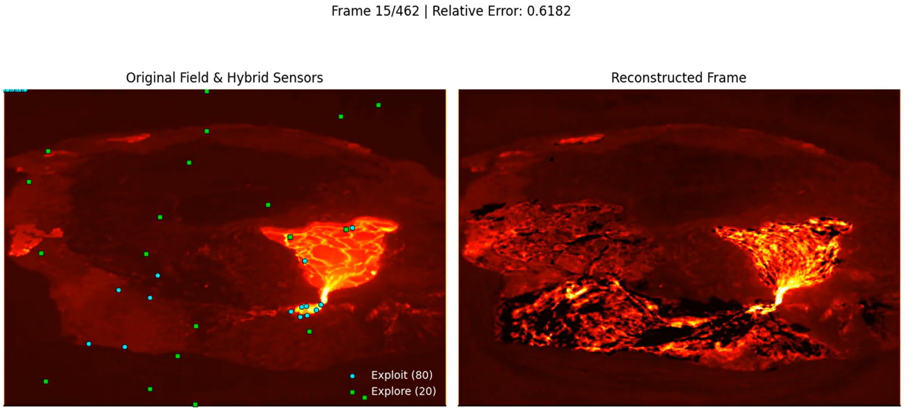

(a) Sensor distribution before convergence, during the initial frames.

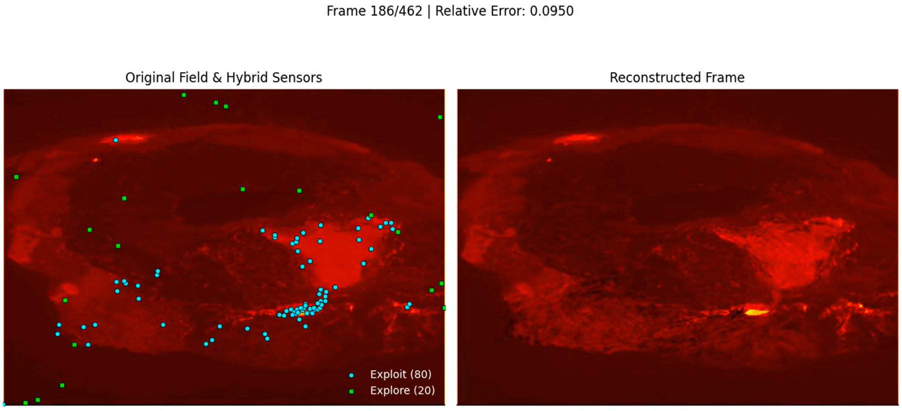

(b) Sensor distribution after convergence, but before the main eruption event.

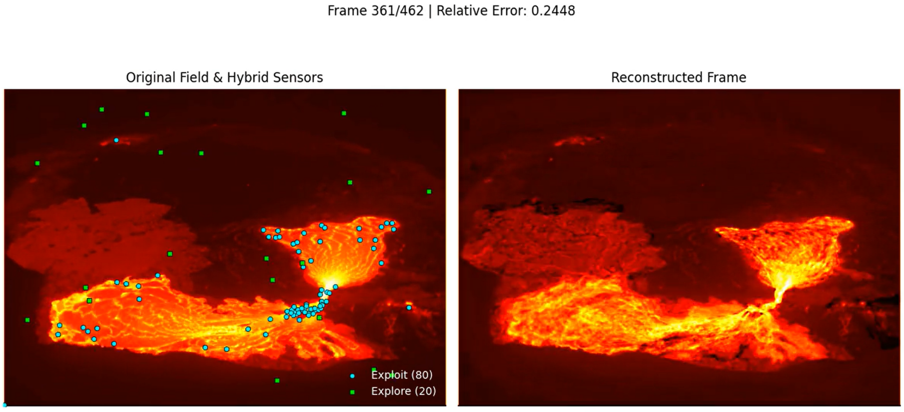

(c) Sensor distribution after the main eruption event, showing limited reconfiguration.

Figure 10. Evolution of the exploitation sensor ($r_{\text{exploit}} = 80$) placement at three distinct stages of the simulation, overlaid on the corresponding thermal video frames.

For this simulation, we set the number of adaptive "exploitation" sensors to $r_{\text{exploit}} = 80$ and the number of random "exploration" sensors to $r_{\text{explore}} = 20$. The sliding window size is $W = 100$, matching the total number of sensors. Crucially, the global reconstruction basis, $\mathbf{U}_{r,\text{global}}$, was trained in an offline phase using only the first 200 odd-numbered frames of the video.

Figure 10 illustrates the evolution of the exploitation sensor placements at three critical time instances of the eruption. The results reveal a distinct pattern of convergence. As the simulation progresses through the first phase of the eruption, the locations of the exploitation sensors rapidly converge to a nearly stable configuration, focusing on the primary areas of lava activity. Once converged, their positions exhibit only minor fluctuations from frame to frame. This rapid convergence in sensor placement corresponds directly to the behavior of the reconstruction error. The relative Frobenius norm error, which starts at approximately 0.5, quickly drops and stabilizes within a range of 0.05 to 0.15. This demonstrates the algorithm's ability to swiftly identify and lock onto the key features of a relatively stable dynamical system. However, as the simulation enters the second phase, we observe that the sensor distribution does not significantly reconfigure, even during the main eruption event. A potential explanation for this inertia is that the window size ($W = 100$) is large relative to the duration of the rapid eruption event, which spans approximately 20 frames. Consequently, the snapshot matrix $\mathbf{G}_{\text{window}}$ that determines the sensor placement $\mathbf{S}_t$ is dominated by pre-eruption data, causing the resulting $\mathbf{S}_t$ to remain largely unchanged. This suggests that increasing the temporal sampling rate of the source video, which would reduce the physical time spanned by the frames within the window, could enhance the sensitivity of the sensor placement $\mathbf{S}_t$ to rapid changes in the flow.

4 Conclusions and Discussions

In this study, we explored both physics-based and data-driven approaches to model and monitor lava flows. The physics-based approach focused on analytically deriving and numerically approximating a reduced-order model that represents lava flow down an incline in one dimension. The analytical model, composed of both short-term and long-term similarity solutions, qualitatively captured expected physical behavior of a highly viscous fluid and showed agreement with the previously modeled corresponding two-dimensional problem. Given these promising initial results, future work may consider further characterization of asymptotic behavior, reconciliation of the short-term and long-term solutions, and a more refined definition of the similarity boundary conditions. Numerical simulations of developed lubrication model presented typical lava flow dynamics both spreading on a flat substrate and down an inclined plane. Moreover, we numerically explored the temperature cooling dynamics within an evolving lava flow, showing both one-dimensional and two-dimensional temperature profiles under different assumptions. It would be of interest to incorporate temperature-dependent viscosity and crust formation in the modeling and numerical study of the lava flow problem in the future.

The data-driven component focused on a critical real-world problem: reconstructing a high-dimensional thermal field from a limited number of sensor measurements. The stationary strategy of placement of sensors, while effective, proved to have two major drawbacks: its sensor locations are inflexible to evolving flow dynamics, and it requires a complete, offline dataset for training. To address these issues, we developed a dynamical algorithm. This online approach removes the need for a complete prior dataset and allows the sensor network to adapt in real-time. By learning from a sliding window of recent sparse measurements, it demonstrates improved flexibility. However, this adaptivity introduces new challenges, such as tuning the algorithm's sensitivity to rapid events, which highlights promising directions for future research in real-time environmental monitoring.

Acknowledgements

We thank Dr. Manuchehr Aminian for running the camp and helpful commentary, the California State Polytechnic University at Pomona for hosting us, and SIAM for funding this camp. We also recognize and appreciate the other participants of GSMMC 2025 for contributing to such a positive and product research environment.

Author Contributions

- Introduction: Darsh Gandhi, Adam Petrucci
- Physics-based modeling
  - Lubrication theory formulation: Kausik Das
  - Similarity solutions:
    - Analytical derivation: Isabelle Sanz (Lead), Kausik Das, Adam Petrucci
    - Numerical implementation: Kausik Das, Adam Petrucci
  - Numerical simulations: Geoffrey Hewitt, Toluwanimi Akinwande
- Optimal sensor placement
  - Stationary optimal sensor placement: Darsh Gandhi, Maria Camila Mejia Garcia, Zhihua Li, Luan Fabricio Lopes
  - Dynamic optimal sensor placement: Zhihua Li (Lead), Luan Fabricio Lopes
  - Numerical implementation: Darsh Gandhi, Maria Camila Mejia Garcia, Zhihua Li, Luan Fabricio Lopes

References

[1] Peter Benner, Serkan Gugercin, and Karen Willcox. A survey of projection-based model reduction methods for parametric dynamical systems. *SIAM review*, 57(4): 483–531, 2015.

[2] Gal Berkooz, Philip Holmes, and John L Lumley. The proper orthogonal decomposition in the analysis of turbulent flows. *Annual review of fluid mechanics*, 25(1): 539–575, 1993.

[3] Tan Bui-Thanh, Murali Damodaran, and Karen Willcox. Aerodynamic data reconstruction and inverse design using proper orthogonal decomposition. *AIAA journal*, 42(8):1505–1516, 2004.

[4] Jared L Callaham, Kazuki Maeda, and Steven L Brunton. Robust flow reconstruction from limited measurements via sparse representation. *Physical Review Fluids*, 4(10):103907, 2019.

[5] Saifon Chaturantabut and Danny C Sorensen. Nonlinear model reduction via discrete empirical interpolation. *SIAM Journal on Scientific Computing*, 32(5):2737–2764, 2010.

[6] Saifon Chaturantabut and Danny C Sorensen. A state space error estimate for pod-deim nonlinear model reduction. *SIAM Journal on numerical analysis*, 50(1): 46–63, 2012.

[7] Francesca Cigna, Deodato Tapete, and Zhong Lu. Remote sensing of volcanic processes and risk. *Remote Sensing*, 12(16), 2020.

[8] Emily Clark, Travis Askham, Steven L Brunton, and J Nathan Kutz. Greedy sensor placement with cost constraints. *IEEE sensors journal*, 19(7):2642–2656, 2018.

[9] Diego Coppola, Marco Laiolo, Corrado Cigolini, Francesco Massimetti, Dario Delle Donne, Maurizio Ripepe, Hidran Arias, Sara Barsotti, Claudia Bucarey Parra, Riky Gustavo Centeno, et al. Thermal remote sensing for global volcano monitoring: experiences from the mirova system. *Frontiers in Earth Science*, 7:362, 2020.

[10] Zlatko Drmac and Serkan Gugercin. A new selection operator for the discrete empirical interpolation method—improved a priori error bound and extensions. *SIAM Journal on Scientific Computing*, 38(2):A631–A648, 2016.

[11] Mohammad Farazmand and Arvind K Saibaba. Tensor-based flow reconstruction from optimally located sensor measurements. *Journal of Fluid Mechanics*, 962:A27, 2023.

[12] US Centers for Disease Control and Prevention. Health effects of volcanic air pollution. URL `https://www.cdc.gov/volcanoes/risk-factors/index.html`.

[13] Sergio Freire, Aneta J Florczyk, Martino Pesaresi, and Richard Sliuzas. An improved global analysis of population distribution in proximity to active volcanoes, 1975–2015. *ISPRS international journal of geo-information*, 8(8):341, 2019.

[14] Kai Fukami, Romit Maulik, Nesar Ramachandra, Koji Fukagata, and Kunihiko Taira. Global field reconstruction from sparse sensors with voronoi tessellation-assisted deep learning. *Nature Machine Intelligence*, 3(11):945–951, 2021.

[15] R.W. Griffiths. The dynamics of lava flows. *Annual Review of Fluid Mechanics*, 32:477–518, 2000.

[16] Renjie Huang, Wen-Zhan Song, Mingsen Xu, Nina Peterson, Behrooz Shirazi, and Richard LaHusen. Real-world sensor network for long-term volcano monitoring: Design and findings. *IEEE Transactions on Parallel and Distributed Systems*, 23(2): 321–329, 2011.

[17] Herbert E. Huppert, John B. Shepherd, R. Harldur Sigurdsson, and Stephen J. Sparks. On lava dome growth, with application to the 1979 lava extrusion of the sourfrière of st. vincent. *Journal of Volcanology and Geothermal Research*, 14:199–222, 1982.

[18] Balaji Jayaraman, SM Abdullah Al Mamun, and Chen Lu. Interplay of sensor quantity, placement and system dimension in pod-based sparse reconstruction of fluid flows. *Fluids*, 4(2):109, 2019.

[19] Roman Lara, Diego Benitez, Antonio Caamano, Marco Zennaro, and Jose Luis Rojo-Alvarez. On real-time performance evaluation of volcano-monitoring systems with wireless sensor networks. *IEEE Sensors Journal*, 15(6):3514–3523, 2015.

[20] John R. Lister. Viscous flows down an inclined plane from point and line sources. *Journal of Fluid Mechanics*, 242:631–653, 1992.

[21] Krithika Manohar, Bingni W Brunton, J Nathan Kutz, and Steven L Brunton. Data-driven sparse sensor placement for reconstruction: Demonstrating the benefits of exploiting known patterns. *IEEE Control Systems Magazine*, 38(3):63–86, 2018.

[22] Stephen R McNutt. Volcanic seismology. *Annu. Rev. Earth Planet. Sci.*, 33(1): 461–491, 2005.

[23] National Geophysical Data Center / World Data Service (NGDC/WDS). Ncei/wds global significant volcanic eruptions database, 2024. URL `https://www.ncei.noaa.gov/products/natural-hazards/volcanoes`.

[24] International Volcanic Health Hazard Network. Hawaii interagency vog information dashboard. URL `https://vog.ivhhn.org/`.

[25] Univeristy of Hawai'i at Hilo. Natural hazards big island: Evacuating during volcanic activity. URL `https://hilo.hawaii.edu/natural-hazards/volcanoes/evacuating.php`.

[26] Ronald L. Panton. *Incompressible Flow*. John Wiley and Sons Inc, 2013.

[27] Dennis E Phillips, Mohammad-Mahdi Moazzami, Guoliang Xing, and Jonathan M Lees. A sensor network for real-time volcano tomography: System design and deployment. In *2017 26th International Conference on Computer Communication and Networks (ICCCN)*, pages 1–9. IEEE, 2017.

[28] Harry Pinkerton and Gill Norton. Rheological properties of basaltic lavas at subliquidus temperatures: laboratory and field measurements on lavas from Mount Etna. *Journal of Volcanology and Geothermal Research*, 68(4):307–323, 1995.

[29] Michael P Poland, Taryn Lopez, Robert Wright, and Michael J Pavolonis. Forecasting, detecting, and tracking volcanic eruptions from space. *Remote Sensing in Earth Systems Sciences*, 3:55–94, 2020.

[30] I Sonder, B Zimanowski, and R Büttner. Non-newtonian viscosity of basaltic magma. *Geophysical research letters*, 33(2), 2006.

[31] Wen-Zhan Song, Renjie Huang, Mingsen Xu, Behrooz Shirazi, and Richard LaHusen. Design and deployment of sensor network for real-time high-fidelity volcano monitoring. *IEEE Transactions on Parallel and Distributed Systems*, 21(11): 1658–1674, 2010.

[32] United States Geoloegical Survey. Hawaiian volcano observatory. URL `https://www.usgs.gov/observatories/hvo`.

[33] Gavin Douglas Tolometti, CD Neish, Gordon R Osinski, Scott S Hughes, and SE Kobs Nawotniak. Interpretations of lava flow properties from radar remote sensing data. *Planetary and Space Science*, 190:104991, 2020.

[34] U.S. Geological Survey Hawaiian Volcano Observatory. February 7–10, 2022, kīlauea summit eruption thermal timelapse video, 2022. URL `https://www.usgs.gov/media/videos/february-7-10-2022-kilauea-summit-eruption-thermal-timelapse-video`.

[35] Yuepeng Wang, Xuemei Ding, Kun Hu, Fangxin Fang, IM Navon, and Guang

Lin. Feasibility of deim for retrieving the initial field via dimensionality reduction. *Journal of Computational Physics*, 429:110005, 2021.

[36] John D Wilding, Weiqiang Zhu, Zachary E Ross, and Jennifer M Jackson. The magmatic web beneath Hawai ‘i. *Science*, 379(6631):462–468, 2023.

[37] Karen Willcox. Unsteady flow sensing and estimation via the gappy proper orthogonal decomposition. *Computers & fluids*, 35(2):208–226, 2006.